

Directional wave climatology for the Hawaiian Islands from buoy data and the influence of ENSO on extreme wave events from wave model hindcast

Jerome Aucan

October 5, 2006

Abstract

A quantitative wave climatology of the Hawaiian Island of O'ahu is derived for northwest and east facing shores, using 4 and 5 years of directional wave buoy data respectively. The northwest facing shores receive swells generated by distant winter North Pacific storms. These swells are highly seasonal, predominant during the months of November to March, and their primary direction is from the NW (315°). The number of extreme swell events during each winter season displays a strong interannual variability, up to a factor of 2 difference from year to year. These northwest swells are almost absent from June to September.

The east facing shores of O'ahu receive waves generated locally and remotely by the easterly trade winds. The trade wind seas in Hawaii originate primarily from NNE (60 to 90°), and are common year-round. Trade wind seas are most likely to be weak in January when they can be replaced by westerly, or Kona winds, while they are notably constant during the summer months of June to September.

The climatology for the northwest swells is extended to the period 1957-2002 with the use of the ECMWF ERA-40 wave model reanalysis. Comparison between the number of high swell events in Hawaii and the Southern Oscillation Index (SOI) indicate that El-Niño years usually experience a larger number of high swell events, while La-Niña years do not show a clear opposite pattern of decreased number of extreme swell events.

Over the period 1957-2002, the average winter wave height in Hawaii increases by 16% and the linear trend of the number of large swells increases from 1 to nearly 3 events per winter season. Averages of winter wave fields over the North Pacific show geographical variations of the highest waves regions, related to different storm genesis regions, storm strength, storm translation speed and directions. During El-Niño years, the central North Pacific experiences the highest wave height field, while during La-Niña years, the highest waves are found near the North American coast.

1 Introduction

The Hawaii archipelago is located in the middle of the tropical North Pacific, and receives a wide range of swells and seas. The 3 main types of waves impacting Hawai'i include the northwest swells generated by north Pacific winter storms, the south swells generated by South Pacific winter storms, and the year-round, easterly, trade-generated seas and swells. Additional sources includes occasional hurricanes and westerly winds (Kona winds).

A directional wave climatology, or the distribution of wave height and direction over time, is a preliminary step to the understanding and study of several coastal geomorphological features. For example, it is widely accepted that the wave climate characteristics are an important factor of coral reef zonation ([1], and others). The number and strength of the extreme swell episodes has also important consequences for the building of man-made offshore structures.

In the state of Hawaii, the official determination of the shoreline reads as follows : "Shoreline means the upper reaches of the wash of the waves, other than storm and seismic waves, at high tide during the season of the year in which the highest wash of the wave occurs, usually evidenced by the edge of vegetation growth, or the upper limit of debris left by the wash of the waves. Hawaii Revised Status, Sect.205A-1". According to the glossary of meteorology, a storm is any disturbed state of the atmosphere, especially as affecting the earth's surface, implying inclement and possibly destructive weather. In Hawaii, however, very large swells generated by north pacific storms can hit the islands, while under clement trade-wind weather. A quantitative wave climatology has therefore direct implications for places such as Hawaii.

The number and strength of high swell events may display an important interannual variability. In the northern hemisphere, it was documented that the frequency and strength of the high latitude storms can be related to some long-term climate indices such as the North Atlantic Oscillation (NAO,[2]), the Pacific Decadal Oscillation (PDO) [3], or the Southern Oscillation Index (SOI). The number of extreme swell events impacting the California has been shown to be correlated to El-Niño events ([4]).

In this study, we first examine several years of data from two Datawell Directional waveriders operated by the University of Hawaii. The position of each buoy relative to the land masses of the archipelago allows for a quantitative study of the statistics of wave height period and direction for the northwest swells and the trade winds swell and seas. In section 2, data from these buoys are analyzed to provide a quantitative estimate of the directional wave climate along the unobstructed north-west and east facing shores of Hawaii archipelago.

In section 3, the data from the buoys are first compared to two global wave model reanalysis (ECMWF ERA-40, and NOAA WaveWatch III) over the period when data and reanalysis overlap. The high wave episodes statistics produced from the ERA-40 reanalysis are then compared with the occurrence and of El-Niño events for the period 1957-2002.

2 Hawaii wave climatology from buoy data

2.1 Data collection and measurement principle

Mokapu Point buoy was first deployed August 9 2000, offshore of Kailua Bay on the windward side of O'ahu, in 120 m water depth. Data from this buoy is archived by the Coastal Data Information Program (CDIP) as station CDIP 098, and by the National Data Buoy Center as station NDBC 51202. Waimea Bay buoy was first deployed December 15 2001, on the northwest facing shores of O'ahu offshore of Waimea Bay, in 200 m water depth (the data is archived as station CDIP 106, or NDBC 51201). Despite the lack of secure operational funding, the Waimea and Mokapu buoys have collected to date an almost uninterrupted dataset of over 4 and 5 years respectively. The gaps in the data were the result of mooring failures, buoy accelerometer failures or computer failures at the shore reception station. The data availability for the two buoys is summarized in table 1 and 2.

The two buoys used in this study are spherical, 0.9 m diameter, Datawell mkII directional waveriders. The buoy hull contains a heave-pitch-roll sensor, a three-axis compass and horizontal accelerometers. After integration, the accelerometers provide the displacement vector, $X(t) = \{X_1(t), X_2(t), X_3(t)\}$, sampled at 1.28 Hz, where the subscripts indicate respectively vertical, west and north displacements. The maximum entropy method (MEM, [5],[6]) is used to calculate the direction/frequency spectrum, $S(\theta, \omega) = E(\omega)D(\theta, \omega)$, Where $E(\omega)$ is the frequency spectrum of the vertical displacement and $D(\theta, \omega)$ is the spreading function. Every half-hour, a complete spectrum is calculated as follows : Displacement timeseries are collected in 200 s blocks (256 samples), and a cosine taper is applied to the first and last 32 samples. This leads to 3 complex Fourier components per frequency ω :

$A_n = \alpha_n + i\beta_n$ with $n = 1, 2, 3$. The cospectra C and quadrature spectra Q are given by :

$$C_{ij} = \overline{A_i} \cdot \overline{A_j} = \alpha_i \alpha_j + \beta_i \beta_j \text{ and } Q_{ij} = \overline{A_i} \times \overline{A_j} = \alpha_i \beta_j - \alpha_j \beta_i \text{ } i, j = 1, 2, 3 \quad (1)$$

For each frequency ω , the coefficients of the directional Fourier series are given by :

$$\begin{cases} a_1 = Q_{12}/[C_{11}(C_{22} + C_{33})]^{1/2} \\ a_2 = (C_{22} - C_{33})/(C_{22} + C_{33}) \\ b_1 = Q_{13}/[C_{11}(C_{22} + C_{33})]^{1/2} \\ b_2 = 2C_{23}/(C_{22} + C_{33}) \end{cases} \quad (2)$$

For each frequency, the directional spreading function $D(\theta)$ can be constructed as :

$$D(\theta) = 1/2\pi(1 - p_1 c_1^* - p_2 c_2^*)/|1 - p_1 e^{-i\theta} - p_2 e^{-2i\theta}|^2$$

where :

$$\begin{cases} c_1 = a_1 + ib_1 \\ c_2 = a_2 + ib_2 \\ p_1 = (c_1 - c_2 c_1^*) / (1 - |c_1|^2) \\ p_2 = c_2 - c_1 p_1 \end{cases} \quad (3)$$

and * denotes a complex conjugate.

The spectra of 8 consecutive blocks(1600 s) are averaged so that a complete directional spectra $S(\theta, \omega)$ is available every half-hour, for :

$$\omega = \begin{cases} 0.025 \text{ Hz} - 0.01 \text{ Hz}, d\omega = 0.005 \text{ Hz} \\ 0.11 \text{ Hz} - 0.58 \text{ Hz}, d\omega = 0.01 \text{ Hz} \end{cases} \quad (4)$$

and $\theta = 0, 5, \dots, 355^\circ$ clockwise relative to true North

For each frequency ω , the mean wave direction is given by $\text{atan}(b_1/a_1)$ and the directional spread by $\sqrt{a_1^2 + b_1^2}$. The peak direction D_p is defined as the mean direction at the peak period $T_p = 1/\omega_p$ for which $E(\omega_p)$ is maximum, and the significant wave height is calculated as :

$$Hsig = 4 \sqrt{\int \int S(\theta, \omega) d\theta d\omega} \quad (5)$$

2.2 Correction for shoaling, refraction, and diffraction

The swells considered in this study include North Pacific storm generated swells, and trade wind generated seas. Both these seas and swells are generated and travel over areas of the North Pacific where the water is deep ($\sim 5000 \text{ m}$) and the deep water approximation for surface gravity waves is valid for all the frequencies of interest (2-25 seconds). In the vicinity of the islands however, we need to take into account the change in wave height H and incidence angle α due to shoaling and refraction. The wave height H_h in water depth h is related to the wave height in deep water H_∞ by $H_h = K_r K_s H_\infty$, where K_r and K_s are the refraction and shoaling coefficient respectively. K_r and K_s are calculated as:

$$\begin{aligned} K_r &= \left(\frac{\cos \alpha_\infty}{\cos \alpha_h} \right)^{1/2} \\ K_s &= \frac{C_{g\infty}}{C_{gh}} \end{aligned} \quad (6)$$

And we calculate the change in wave incidence angle α as

$$\alpha_h = \text{asin} \left(\frac{C_{ph}}{C_{p\infty}} \sin \alpha_\infty \right) \quad (7)$$

Where C_p indicates the wave phase velocity, C_g is the wave group velocity, in deep water (∞) and in water of depth h . The water depths at the Waimea buoy and at the Mokapu buoy are 200 m and 120 m , respectively. The deep water approximation cannot be applied for all frequencies at these depths, and the complete dispersion relation is used to calculate C_{gh} and C_{ph} .

The wave heights and directions show little change between deep water and the buoy locations (figure 2). For Waimea buoy, the change in incidence angle α due to refraction is less than 1° for waves of 17 s period or less. The change in wave height due to shoaling is less than 2% for waves of 17 s period or less. For Mokapu buoy, the change in incidence angle from deep water wave conditions due to refraction is less than 1° for waves of 15 s period or less. The change in wave height due to shoaling is less than 4% for waves of 15 s period or less (figure 2).

The process of wave diffraction operates in regions where refraction creates a gradient of wave height along the direction perpendicular to the wave ray, or along the wave crest. Diffraction transmits energy from area of high energy to areas of low energy. In our case, refraction is minimal, so the effect of diffraction at the buoy locations is considered negligible.

2.3 Northwest swells at Waimea Buoy

2.3.1 Directional climatology

We first investigate the general characteristics of the incoming northwest swells. The directional spectrum at the Waimea buoy is averaged over each available month (figure 3). Due to the position of the Waimea buoy relative to the island of O’ahu, we only use the Waimea buoy to investigate the northwest swells originating between the W and NNE directions. The northwest swells are predominant during the months of October to March (figure 3), with a maximum in January. Their direction is predominantly from the NW (315° , figure 3), and the associated period between 10 and 20 s. At the location of Waimea buoy, the shore normal direction is approximately 300° relative to true North. According to figure 2, the predominant swells measured at the buoy (300° to 330° , 10 to 20 s) underwent a change in wave height and a change of incidence angle below 5% and 1° respectively compared to their deep water characteristics. We consequently conclude that the average directional wave climate measured at the Waimea buoy is representative of an open ocean location offshore of Hawaii, unobstructed for waves originating from the 300° to $\sim 25^\circ$ relative to true north. The island of Kauai blocks swells that originate from directions around 290° . It is unclear to what extent the decrease of energy south of the 300° sector is due to the presence of the island or due to the storm paths in the North Pacific favoring waves in Hawaii coming from the 315° sector. Since 2005, the National Data Buoy Center upgraded station 51001, located 170 nm West Northwest of Kauai Island, to a directional wave buoy. In the future, data from this buoy, coupled with a local wave modelling effort, could quantify the two effects.

A second energy peak is clearly visible year-round in the NE quadrant, and is associated with the trade wind swells and seas. The Waimea buoy is not completely sheltered from the trade wind swells by the island of Oahu, but these swells and seas have undergone significant directional change (20 to 40°) by the time they are measured by the buoy. The trade wind swell and seas will be discussed in more details in the following section using the Mokapu buoy.

In January, there is also noticeable energy in the SW to NW quadrant, at lower period (5 to 10 s, figure 3), that is associated with locally generated seas from the SW to NW direction (Kona Winds conditions).

2.3.2 Extreme events distribution

To investigate the distribution of swell heights on the northwest facing shores, we calculate the wave height corresponding to this particular directional quadrant. In this section we focus on the NW quadrant at Waimea buoy, and calculate $Hsig_{NW}$ by integrating the directional spectrum $S(\theta, \omega)$ over the W to NNE quadrant, for all available frequencies.

$$Hsig_{NW} = 4 \sqrt{\int_{\theta=270^\circ}^{\theta=22.5^\circ} \int_{\omega=0.025 Hz}^{\omega=0.58 Hz} S(\theta, \omega) d\theta d\omega} \quad (8)$$

For consistency with the wave models sampling intervals, we use a 3-hour average of $S(\theta, \omega)$ to calculate $Hsig_{NW}$.

For each month, we calculate the mean wave height, and the percentage distribution of given wave heights (figure 4). The highest average wave height occurs in January, when $\overline{Hsig_{NW}} = 2.4 m$. In January $Hsig_{NW} > 3 m$, 25% of the time and $Hsig_{NW} < 1 m$ only 5% of the time. In sharp contrast, the lowest average $\overline{Hsig_{NW}}$ occur in July when $\overline{Hsig_{NW}} = 0.5 m$ and $Hsig_{NW} < 1 m$, more than 95% of the time.

A typical year can be divided in 4 seasons (Figure 4). The winter season (November to March), when the occurrence of high swell event ($\geq 3 m$) is high, 2 transitional seasons (April, May and October), when moderate swells (1 to 3 m) are common, and a low season when waves are typically $\leq 1 m$ in June, July, August and September. In terms of the shoreline definition, it is obvious that the highest reach of the waves should be estimated during the period of November to March.

2.4 Trade winds swell and seas from Mokapu Buoy

2.4.1 Directional climatology

The Mokapu buoy is used to investigate the climatology of the trade winds swell and seas, that originate from the SE to NNE directions. The trade wind sea directional spectrum shows a predominant energy peak between 6 and 12 s periods and 60 to 90° direction relative to true north, all year-round (figure 5). Compared to the northwest swells, this pattern shows less variations from month to month during the period observed (2001-2005). The northwest swells described in the previous section are also clearly visible at Mokapu buoy, but undergo significant refraction, and will not be discussed here any further. A third peak of energy is visible in the average for the month of November (figure 5), at long periods ($\sim 20 s$), from the NNE. This is due to one extremely high event in November 2003, that caused damages to houses, beach closures and flooded roadways. According to local elders, this had not been seen since 50

years. This swell was not higher than the other high swell originating from the northwest, but its direction made it a very unusual event in Hawaii.

2.4.2 Events distribution

We now focus on the east quadrant at Mokapu buoy. We calculate $Hsig_E$ by integrating the 3-hourly averages directional spectrum $S(\theta, \omega)$ over the E quadrant:

$$Hsig_E = 4 \sqrt{\int_{\theta=22.5^\circ}^{\theta=135^\circ} \int_{\omega=0.025 Hz}^{\omega=0.58 Hz} \overline{S(\theta, \omega)} d\theta d\omega} \quad (9)$$

In January, the average wave height $\overline{Hsig_E}$ from the trade wind seas is the smallest ($\sim 1 m$, figure 6). In January, the trades can also be absent for long periods of time, as they are replaced by westerly (or Kona) winds. Over the observed period, the wave height in January for the trade wind seas is $\leq 1 m$ 56% of the time. During the summer, from June to September, trade wind seas are very constant, with $1 \leq Hsig_E \leq 2 m$, over 75% of the time (figure 6), with a maximum in July (90% of the time).

3 Interannual variability of extreme events in Hawaii

3.1 Wave model reanalysis

The timeserie of buoy data in Hawaii (5 years) is too short to investigate the interannual variability of extreme events in the context of large scale climate indices. To extend the time series of wave height in Hawaii, two different wave model reanalyses are used. Both model are based on the WAM wave model ([7]), use the same basic physics, but different wind forcing products.

The National Centers for Environmental Prediction of the National Oceanic and atmospheric Administration (NCEP/NOAA) provides a global historical wave model on a 1.25° latitude \times 1° longitude grid. This model is called the NOAA WaveWatch III or WW3 ([8]). Historical reanalysis data are available every 3 hours from January 30 1997.

The European Center for Medium-range Weather Forecasting (ECMWF) produced a global wave reanalysis (ERA-40,[9]) on a 1.5° latitude \times 1.5° longitude grid, for the period 1957-2002. The wave model was forced by hourly winds, and output was available every 6-hours.

For each model, the significant wave height $Hsig$, peak wave period T_p and peak wave direction D_p are extrapolated from the global wave fields at each time step, at a point north of Oahu, Hawaii (figure 1, $22^\circ N, 158^\circ W$). WW3 archive does not include time series of directional spectrum, and no funding was available at the time to obtain time series of directional spectrum near Hawaii from the ERA-40 reanalysis. Therefore, directional climatologies from the wave

models similar to the ones obtained from buoy data on figures 5 and 3 are not possible at this time.

3.2 Extreme events

It is apparent on figures 5 and 3 that the directional wave spectrum in Hawaii during the winter is usually bimodal, with one peak at low-frequency from the northwest, and one peak at high frequency from the east. Significant wave heights $Hsig$ from the wave models are calculated with all frequencies and directions. If no swell other than the northwest swell and the trade wind sea is present in the area, then by definition

$$Hsig^2 = Hsig_{NW}^2 + Hsig_E^2 \quad (10)$$

During extreme winter events however, the contribution of $Hsig_E^2$ to $Hsig$ is small ($Hsig_{NW}^2 \gg Hsig_E^2$), so we can compare $Hsig_{NW}^2$ from the buoy, to $Hsig$ from the model reanalysis. To prevent identification of south swells or easterly swells, we only keep the $Hsig$ from the model reanalysis when the corresponding peak wave direction D_p satisfies $D_p \leq 25^\circ$ or $D_p \geq 270^\circ$. To identify an individual swell, we use the daily average of wave height from the buoy and the model and identify local maxima. For each winter season, the number of large swell events ($Hsig > 4m$) is calculated from the two models and the Waimea Buoy (figure 7). Over the period 1997-2001, the two models produces the same number of extreme events (to within 1 event). Over the period 2001-2004, when model and buoy data overlap, there are larger differences between the numbers of events produced by the model or the buoy timeserie (figure 7). The differences can be due to inherent errors in the wave models, or related the different methods for calculating wave height. When available, this analysis should be redone using the directional spectrum time series from the ERA-40 reanalysis. Nonetheless, we will use the extreme events statistics from the ERA-40 wave model in the following section.

3.3 Long term trend and relation to climate indices

To estimate the influence of El-Niño, we calculate the average Southern Oscillation Index (SOI) for each winter season (November to March), and compare with the number of large events in Hawaii from the ERA-40 model, and the WW3 model (figure 8). The SOI climate index was obtained from the National Oceanic and Atmospheric Administration/ Cooperative Institute for Research in Environmental Sciences (NOAA/CIRES) Climate Diagnostic Center (CDC). The Southern Oscillation Index (SOI) is defined as the normalized pressure difference between Tahiti and Darwin. There are several slight variations in the SOI values calculated at various centres. Here we use the SOI from the Climate Research Unit (CRU) at the University of East Anglia, which is based on the method given by [10]. A negative SOI indicates an El-Niño event, while a positive SOI indicates a La Niña event. Here, we arbitrarily define El-Niño events when the winter average of SOI is $SOI \leq -1$, and Niña event when $SOI \geq 0.5$.

We extend the calculation of extreme events ($H_{sig} > 4 m$) to the 1957-2002 period, using the timeserie of wave height produced by the ERA-40 reanalysis (figure 8). The number of extreme events for each winter season (November-March) varies significantly from year to year, from 7 events during the strong El-Niño period of 1997-1998, to no events at all. The number of extreme events from the ERA-40 reanalysis shows a significant increasing linear trend over the period 1957-2002 (figure 8), from just over 1 major event per season in 1958 to over 3 events per season in 2001. Over the period 1957-2002, the significant wave height averaged for each winter season (November to March) shows a 16% increase. This is consistent with the intensification of North Pacific Winter Cyclones ([3] and others). If we add the period 2002-2005 (figure 7), the increasing trend will likely be even more pronounced. During all El-Niño events (65-66,77-78,82-83,86-87,91-92,97-98), Hawaii experience more extreme events than the average trend (figure 8). La-Niña years do not necessarily coincide with less extreme events.

An increase of the number of high swell events over the same period was also documented in California ([4]). This increase may be related to the average wave field in the North Pacific. We use our arbitrary threshold for defining SOI state (figure 8) to produce winter averages (November-March) of wave height from the ERA-40 reanalysis over the North Pacific, for the two extreme SOI conditions (figure 9 top and bottom), and for the overall average (figure 9 middle). The wave heights averaged over the winters of strong El-Niño are higher than the average (figure 9). Differences in wave height reach up to 1 m in the central North Pacific between El-Niño years average and the overall average. Differences in wave height between the La-Niña years average and the overall average are not as large.

The time-averaged wave height field shows different geographical distribution (figure 9) during El-Niño or La-Niña years. The overall average for the 1957-2002 period (figure 9 middle) shows two areas of increased wave height, the first in the central North Pacific, centered around $40^{\circ}N$ and $175^{\circ}W$, and a second one offshore of North America, near $45^{\circ}N$ and $135^{\circ}W$. During El-Niño years (figure 9 top), the central Pacific high wave area is predominant, and no secondary maximum in wave height is observed near the North American coast. During La-Niña years (figure 9 bottom), the North American coast region experiences the highest time-averaged wave heights.

The wave heights are not only related to the wind speed during a storm, but also to the storm translation speed and direction ([11]). The differences in the geographical distribution of high wave height between El-Niño and La-Niña years indicate differences in the combination of cyclogenesis regions and storms intensities and trajectories. A more in-depth description of the physical mechanisms explaining these differences is out of the scope of this paper.

4 Summary and discussion

We have described the wave climate for the northwest and east facing shores of the Island Of Oahu, Hawaii, with data from 2 different buoys (figures 3 to 6). This wave climatology quantifies the average wave energy received by each shore, and will be useful for the studies of biological and physical processes where wave play an active role. A direct comparison of this measurement-based directional wave climatology with the results of two widely used wave model products (WaveWatch III and ERA-40) was not possible because of the unavailability of directional spectrum time-serie from the models.

We use the results from the wave models to extend the northwest extreme events climatology to the period 1957-2002 (figure 8). We found that the number of extreme events (larger than 4 m) increased over the period, and that during El-Niño years, Hawaii experiences a larger number of extreme events. Maps of time-averaged wave height in the North Pacific also show higher basin-wide wave heights during El-Niño years. The geographical distribution of high wave heights is different during El-Niño and La-Niña years (figure 9), and is likely related to a combination of different cyclogenesis regions and different storms intensities and trajectories

Acknowledgments

The directional waverider buoys used in this study were purchased through a DURIP grant from the Office of Naval Research. Funding for the maintenance of the buoys, and the salary of the author were provided by Dr. Mark Merri-field, director of the University of Hawaii Sea-Level-Center (UHSLC), through the Joint Institute of Marine and Atmospheric Research (JIMAR). The staff at the Coastal Data Information Program (CDIP), and Julie Thomas in particular, provided invaluable technical advice and were responsible for the data acquisition and archiving of the buoys. ERA-40 data was retrieved from the online catalog of the European Center for Medium-Range Weather Forecasts (ECMWF).

References

- [1] R. W. Grigg. Holocene coral reef accretion in hawaii: A function of wave exposure and sea level history. *Coral Reef*, 17:263–272, 1998.
- [2] D. K. Woolf, P. G. Challenor, and P. D. Cotton. Variability and predictability of the North Atlantic wave climate. *Journal of Geophysical Research (Oceans)*, 107:9–1, October 2002.
- [3] N.E. Graham and H.F. Diaz. Evidence for intensification of north pacific winter cyclones since 1948. *bams*, 2001.

- [4] R. Seymour. Wave climate variability in southern california. *J. Wtrwy., Port, Coast., and Oc. Engrg.*, 122(4):182–186, 1996.
- [5] A. Lygre and H. Krogstad. Maximum entropy estimation of the directional distribution in ocean wave spectra. *J. Phys. Oceanogr.*, 16:2052–2060, 1986.
- [6] R. B. Long. The statistical evaluation of directional spectrum estimates derived from pitch/roll buoy data. *J. Phys. Oceanogr.*, 1980.
- [7] WAMDI. The wam model-a third generation ocean wave prediction model. *J. Phys. Oceanogr.*, 18:1775–1810, 1988.
- [8] H. L. Tolman. User manual and system documentation of wavewatch-iii version 1.18. Technical report, Ocean Modeling Branch, NCEP, National Weather Service, NOAA, Department of Commerce, 1999.
- [9] S. Caires, A. Sterl, J.R. Bidlot, N. Graham, and V. Swail. Intercomparison of different wind-wave reanalyses. *J. Climate*, 17:1893–1913, 2004.
- [10] C.F. Ropelewski and P.D. Jones. An extension of the Tahiti-Darwin southern oscillation index. *Month. Weath. Rev.*, 115:2161–2165, 1987.
- [11] J. Wolf and D.K. Woolf. Waves and climate change in the north-east Atlantic. *Geophys. Res. Letters*, 2006.

Tables

	Jan	Feb	Mar	Apr	May	Jun	Jul	Aug	Sep	Oct	Nov	Dec
2000	0%	0%	0%	0%	0%	0%	0%	30%	100%	93%	80%	100%
2001	100%	100%	100%	100%	100%	100%	100%	100%	100%	100%	100%	100%
2002	100%	100%	100%	100%	100%	100%	100%	100%	100%	100%	100%	100%
2003	100%	100%	100%	100%	100%	100%	100%	100%	100%	100%	100%	100%
2004	100%	57%	0%	0%	35%	100%	100%	93%	100%	100%	100%	100%
2005	100%	100%	100%	100%	100%	100%	100%	100%	100%	100%	100%	100%

Table 1: Mokapu Point buoy availability, in percent

Figures

	Jan	Feb	Mar	Apr	May	Jun	Jul	Aug	Sep	Oct	Nov	Dec
2000	0%	0%	0%	0%	0%	0%	0%	0%	0%	0%	0%	0%
2001	0%	0%	0%	0%	0%	0%	0%	0%	0%	0%	0%	51%
2002	100%	100%	100%	100%	100%	100%	100%	93%	80%	97%	100%	100%
2003	100%	100%	100%	100%	100%	100%	66%	0%	0%	38%	86%	100%
2004	100%	100%	100%	100%	100%	100%	100%	100%	100%	97%	83%	100%
2005	100%	100%	100%	100%	100%	100%	100%	100%	100%	100%	100%	100%

Table 2: Waimea Bay buoy availability, in percent

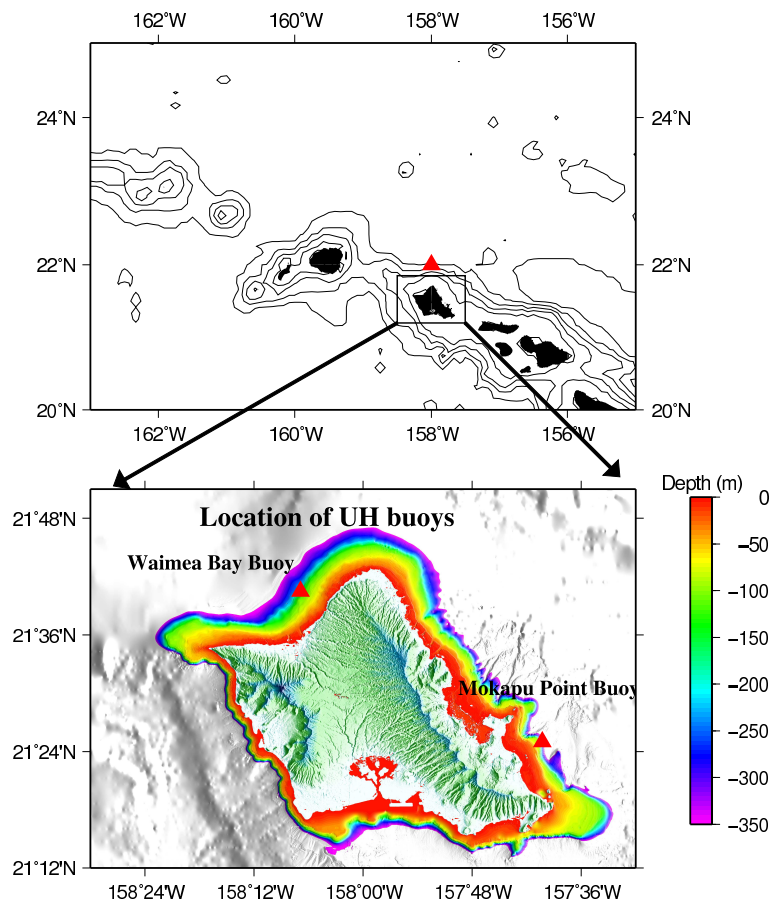


Figure 1: Top : Location map of the Hawaiian Islands chain, and wave model output (red triangle). Bottom : Bathymetry of Oah'u and location of the wa-verider buoys (red triangles)

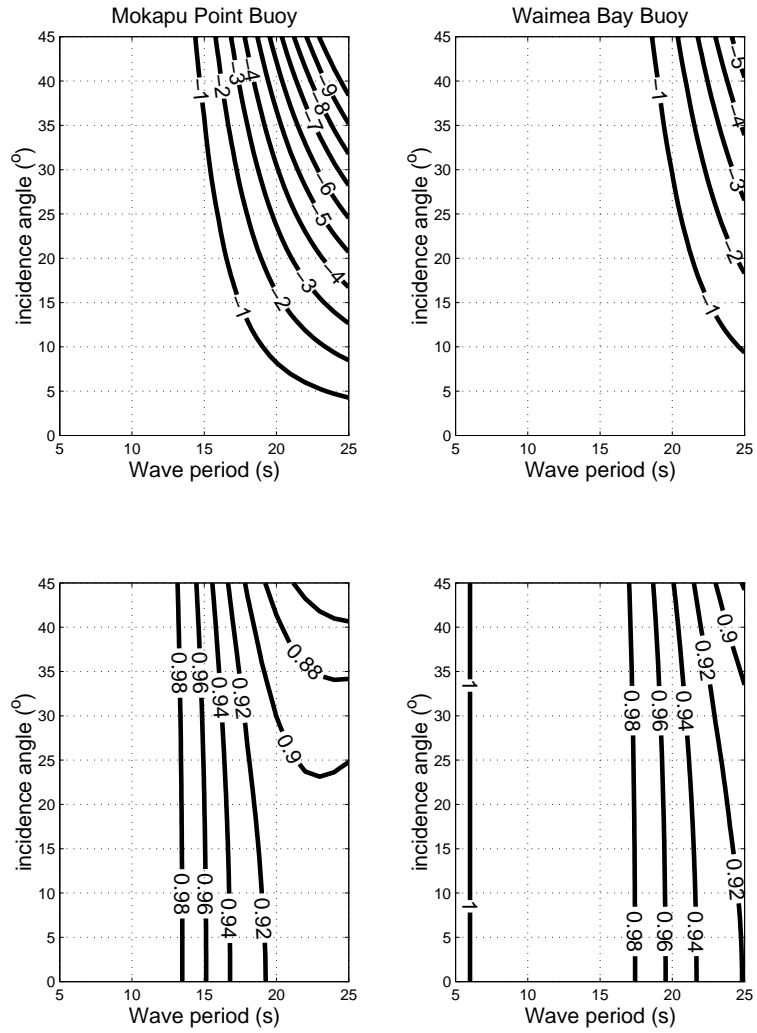


Figure 2: Effect of refraction between deep water and the depth at the buoy location for Mokapu Point buoy (left) and Waimea Bay buoy (right). Change of angle of incidence (degree) as a function of deep water incidence angle and wave period (top), and refraction and shoaling coefficient ($K_r K_s$) as a function of deep water incidence angle and wave period (bottom)

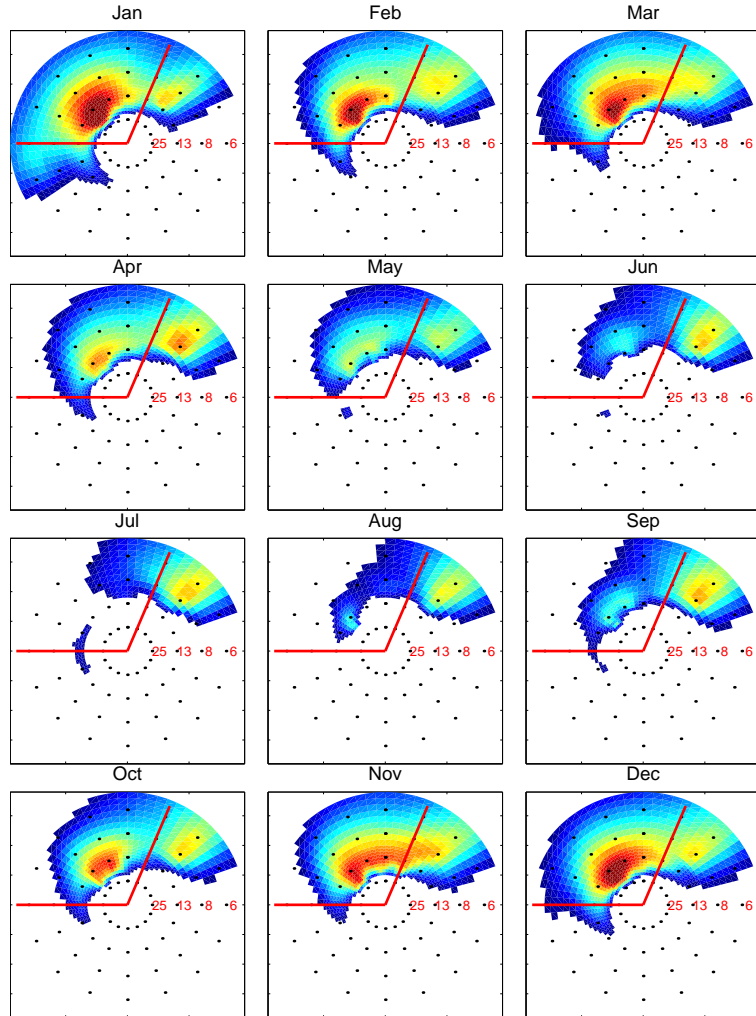


Figure 3: Averages of directional spectra for each months at Waimea Bay buoy. color scale is logarithmic, constant over all frames, and covers 2 orders of magnitude. Values that are a factor 3 smaller than the maximum are not plotted. Red lines show the sector of the origin of waves used for the calculation of $Hsig_{NW}$

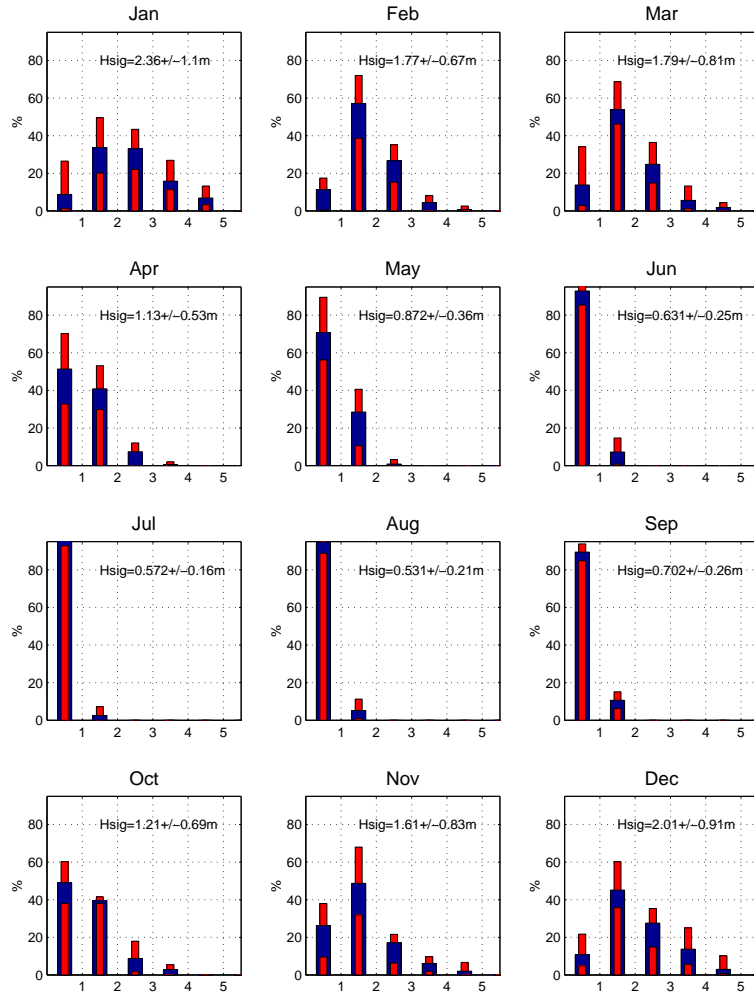


Figure 4: Histograms of occurrence (in percent of time) of wave height $Hsig_{NW}$ for each months at Waimea buoy. Blue bars indicate the mean for each month when calculated over all the available years, and red bars indicate minima and maxima for each month and wave size. Mean wave height is indicated for each month plus or minus one standard deviation.

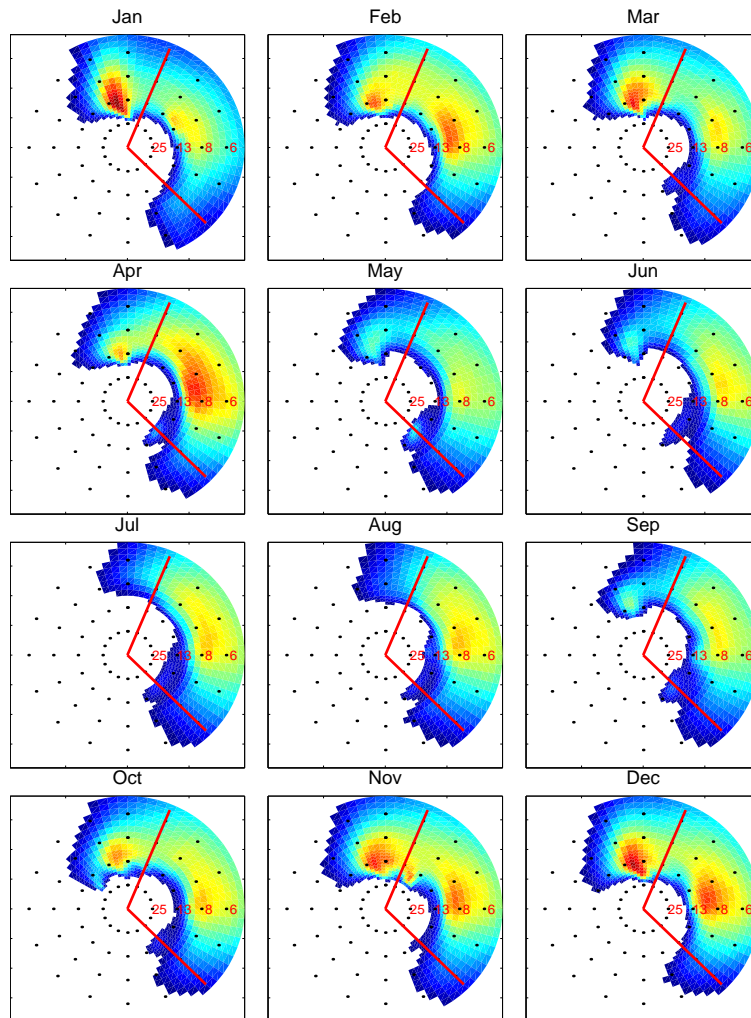


Figure 5: Averages of directional spectra for each months at Mokapu Point buoy. color scale is logarithmic, constant over all frames, and covers 2 orders of magnitude. Values that are a factor 3 smaller than the maximum are not plotted. Red lines show the sector of the origin of waves used for the calculation of $Hsig_E$

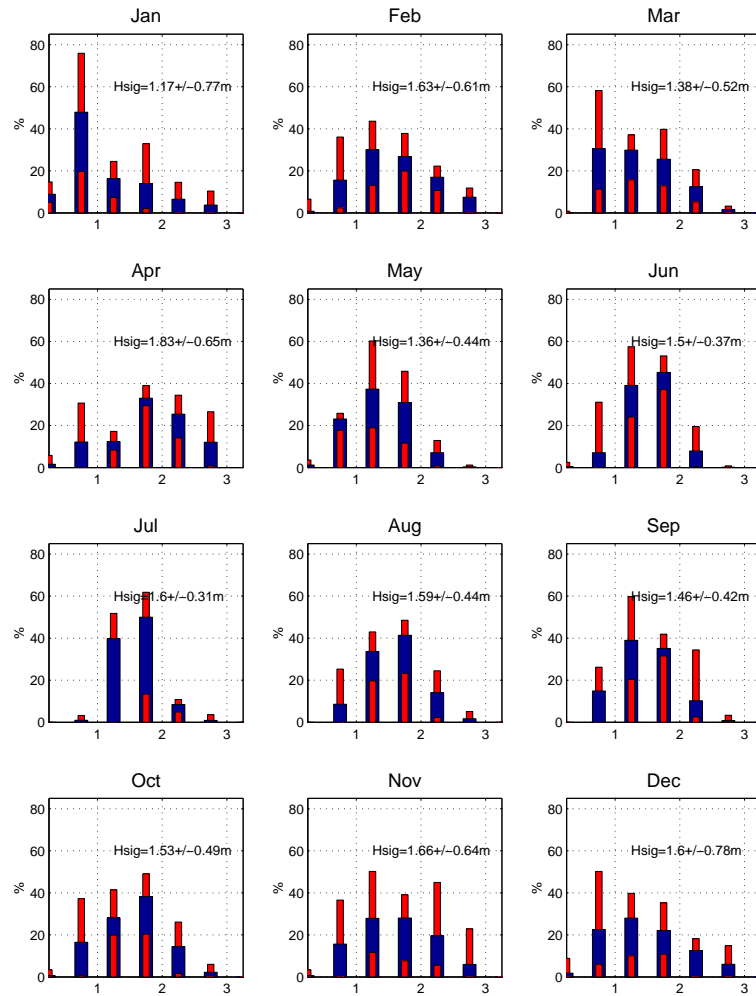


Figure 6: Histograms of occurrence (in percent of time) of wave heights H_{sig_E} for each months at Mokapu buoy. Blue bars indicate the mean for each month when calculated over all the available years, and red bars indicate means and max for each month and wave size. Mean wave height is indicated for each month plus or minus one standard deviation.

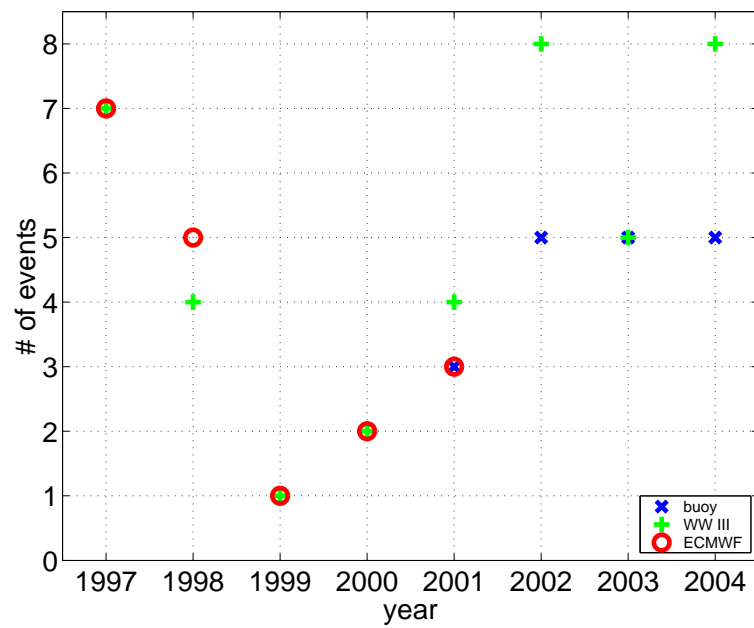


Figure 7: Number of extreme swell events ($\geq 4m$) for each winter season (November to March), for the NW quadrant, from the ERA-40 model (red), WW3 model (green) and the Waimea Buoy (blue) data

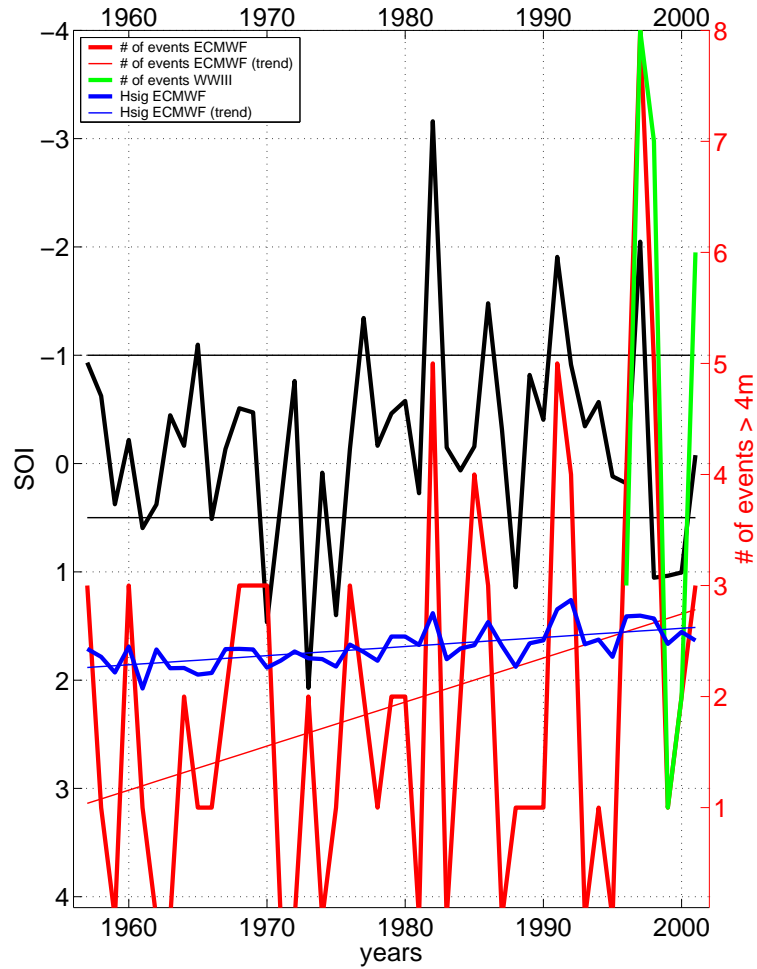


Figure 8: Time series of Southern Oscillation Index (SOI), averaged for each winter season (November-March, black line). The thin black lines represent the arbitrary threshold for defining El-Niño and La-Niña years. time series of the number of extreme swell events ($\geq 4m$) from the ERA-40 reanalysis (red) and WW3 (green). The thin red line represent the linear trend for the number of events from the ERA-40 reanalysis. The average significant wave height in Hawaii for each winter season (November-March) is indicated in thick blue, and its linear trend in thin blue.

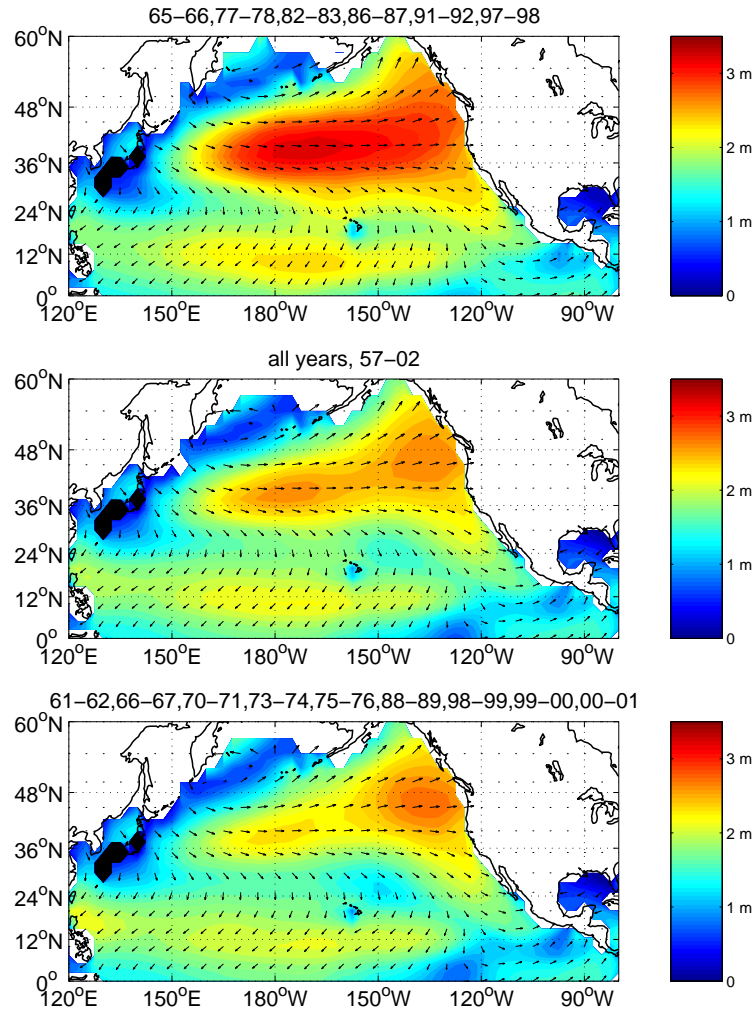


Figure 9: Average wave height and direction from ECMWF ERA-40, for the months of November to March, averaged for all El-Niño year (top), (winters 65-66,77-78,82-83,86-87,91-92,97-98, averaged for all years from 1957 to 2002 (middle), and averaged for La-Niña years (bottom) (winters 61-62,66-67,70-71,73-74,75-76,88-89,98-99,99-00,00-01). See figure 8, and section 3 for the definition of El-Niño and La-Niña years.